Tribology International 143 (2020) 106041

Contents lists available at ScienceDirect

Tribology International

journal homepage: http://www.elsevier.com/locate/triboint

# Effect of single- and multi-scale surface patterns on the frictional performance of journal bearings – A numerical study

Florian König [a,*], Andreas Rosenkranz [b], Philipp G. Grützmacher [c], Frank Mücklich [c], Georg Jacobs [a]

[a] Institute for Machine Elements and Systems Engineering, RWTH Aachen, 52062, Aachen, Germany
[b] Department of Chemical Engineering, Biotechnology and Materials, University of Chile, Santiago, Chile
[c] Department of Functional Materials, Saarland University, 66123, Saarbrücken, Germany

ARTICLE INFO

*Keywords:*
Journal bearings
Multi-scale patterns
Mixed-elastohydrodynamic simulation
Hot micro-coining
Direct laser interference laser patterning

ABSTRACT

The present study aims at numerically predicting the frictional performance of journal bearings with single- and multi-scale surface patterns considering the real 3D surface topographies after wearing-in in mixed-elastohydrodynamic (mixed-EHL) simulations using a multi-body simulation (MBS) environment. For this purpose, the extended Reynolds equation with flow factors according to Patir and Cheng has been combined with a deterministic asperity contact model, which can be further utilized in the design process to optimize the tribological response of engineering systems. For all patterned surfaces, a shift to smaller rotational speeds in the transition from mixed to hydrodynamic lubrication with a notably reduced coefficient of friction has been demonstrated. The largest frictional improvement (- 80%) has been achieved with single-scale surface patterns fabricated by direct laser interference patterning.

## 1. Introduction

In times of continuously increasing temperatures and $CO_2$-emissions, the desire to provide more sustainable strategies to circumvent these problems has become more important than ever. In the last 30 years, surface patterning has gained notable attention due its tremendous potential to reduce friction and wear. Etsion and his co-workers established the basis of surface patterning applied to tribological problems using experimental and numerical approaches [1,2]. Afterwards, numerous groups have explored the potential of surface patterning to optimize tribological properties under dry and lubricated conditions [1–4]. Several mechanisms have been identified such as the reduction of the real contact area [5,6], the storage of wear debris [7,8], the storage of lubricant (secondary oil effect) [9–12], the build-up of an additional hydrodynamic pressure [13–18] and the possibility to initiate pressure-induced reactions to form tribo-layers [19,20]. Comprehensible reviews about the underlying mechanisms have been published by Hsu et al. [3] and Gachot et al. [21,22]. Based upon these reviews, it can be derived that there are still some remaining questions regarding the underlying mechanisms and effects responsible for an improvement of the tribological properties under mixed and boundary lubrication, which bear potential for more detailed research.

Reviewing the aforementioned articles reveals that mostly purely single-scale patterns have been investigated experimentally and numerically. However, nature provides a number of impressive strategies based upon multi-scale/hierarchical surface patterning such as self-cleaning and superhydrophobicity of the Lotus leaf [23,24], tunable adhesion of the Gecko feet [25,26], interference phenomena on butterfly wings [27,28] or drag reduction for shark skin [29,30]. Following this idea, it seems to be straightforward to postulate that multi-scale surface patterns are effective to optimize friction and wear. A detailed review of the literature although reveals that tribological properties of multi-scale patterns are largely underexplored [31]. Nevertheless, a few manuscripts can be found addressing the effect of multi-scale patterns on friction and/or wear. Segu et al. verified the possibility to reduce friction by multi-shape patterns having circular and elliptical features [39]. Hsu et al. investigated different pattern geometries under light low load and high speed conditions as well as severe high load and low speed conditions. Related to low load and high speed conditions, elliptical patterns oriented perpendicular to the sliding direction have led to the greatest friction reduction under boundary and mixed lubrication. Under high load and low speed conditions, patterns induced detrimental effects with increased friction due to undesired edge effects [3].

* Corresponding author.
*E-mail address:* florian.koenig@imse.rwth-aachen.de (F. König).

https://doi.org/10.1016/j.triboint.2019.106041
Received 23 August 2019; Received in revised form 15 October 2019; Accepted 26 October 2019
Available online 30 October 2019

**Nomenclature**

*Latin letters*

| | |
|---|---|
| $A$ | Nominal contact area, $m^2$ |
| $A_a$ | Real contact area, $m^2$ |
| $A_f$ | Contact area of single asperity contact, $m^2$ |
| $F_f$ | Friction force, N |
| $F_R$ | Radial force, N |
| $\overline{h}$ | Average film thickness, m |
| $h$ | Nominal film thickness/surface separation, m |
| $h_{oil}$ | Minimum nodal oil film thickness, m |
| $p_a$ | Asperity contact pressure, Pa |
| $p$ | Oil film pressure, Pa |
| $P_f$ | Single asperity contact force, N |
| $p_{Asperity}$ | Maximum nodal asperity contact pressure, Pa |
| $p_{oil}$ | Maximum nodal oil film pressure,Pa |
| $u$ | Linear velocity, m/s |
| $r$ | Bearing radius, m |
| $R_a$ | Mean roughness, m |
| $R_q$ | Root mean square (RMS) roughness, m |
| $R_z$ | Surface roughness, m |
| $t$ | Time, s |
| $u$ | Sliding velocity, m |
| $z_s$ | Summit height, m |

*Greek letters*

| | |
|---|---|
| $\eta$ | Dynamic viscosity, Pa·s |
| $\varphi$ | Flow/shear/contact factor |
| $\phi$ | Bearing angle, deg |
| $\sigma$ | Surface roughness, m |
| $\theta$ | Fill ratio |
| μ | Boundary friction coefficient |
| $\phi_s$ | Density distribution of all summit heights, m |
| $\tau_a$ | Asperity shear stress, Pa |
| $\tau_h$ | Viscous shear stress, Pa |
| $\eta_s$ | Asperity density |

*Abbreviations*

| | |
|---|---|
| COF | Coefficient of friction |
| DLIP | Direct laser interference pattering |
| MC | Micro-coining |
| MULTI | Multi-scale surface pattern (MC+DLIP) |
| REF | Reference |

*Subscripts*

| | |
|---|---|
| 1 | Journal |
| 2 | Bearing |
| x | Sliding direction |
| y | Cross direction |

Following this systematic study on single-scale patterns, Hsu et al. combined small but deep patterns with large but shallow patterns to be effective under different lubricated conditions. They also created a mixture of patterns on different scales following design rules found in nature, which favor overlapping patterns on different scales. Especially, overlapping multi-scale patterns showed a maximum friction reduction of up to 80% with negligible wear [32].

By a combination of diamond cutting and shot blasting, Resendiz et al. manufactured multi-scale patterns on aluminum. Under lubricated conditions, these surfaces demonstrated synergetic effects with beneficial frictional properties [33]. Wang et al. studied SiC bearings with multi-scale patterns under water lubrication thus demonstrating that they can withstand higher critical loads until the initiation of severe wear [34]. Grützmacher et al. verified a beneficial friction behavior of multi-scale patterns fabricated by hot micro-coining and direct laser interference patterning (DLIP) in lab experiments and applied to journal bearings [35,36]. Especially, under mixed and full-film hydrodynamic lubrication, the multi-scale patterns demonstrated significantly reduced friction [36]. Rosenkranz et al. studied the maximum oil film lifetime of single- and multi-scale patterns fabricated by DLIP and micro-coining. The longest oil film lifetime has been found for the sample with the deepest and widest micro-coined patterns combined with the finer cross-like laser pattern [37].

Apart from experimental studies, numerical work can significantly facilitate the design and optimization of multi-scale patterns. Two modelling approaches including computational fluid dynamics (CFD) and Reynolds-type equation modeling are commonly used to assess the frictional performance of surface patterns [38–40]. Potential advantages of numerical approaches based upon the Reynolds' equation are the lower computational cost required to simulate patterned contacts compared to full CFD methods as well as the existence of numerous modified versions to incorporate effects such as cavitation, turbulent flows, lubricant rheology, and surface roughness. Hu and Zhu [41–45] presented a fully coupled mixed-EHL model to assess the frictional behavior of multi-scale patterns. This model was applied to provide a virtual surface patterning simulation tool to predict innovative pattern designs under mixed lubrication in non-conformal contacts. It was shown that the frictional performance is strongly influenced by the pattern design and density [46,47]. Patir and Cheng [48,49] presented an average flow model for surface roughness patterns by incorporating "flow factor" coefficients in a modified Reynolds equation. The Patir and Cheng average flow model has proven to be effective to predict the mixed lubrication performance for a wide range of tribological applications. Regardless of the tribological application, an important aspect for the efficient use of any average flow model refers to the proper calculation of the flow factor coefficients for a specified topography [50–57]. Semi-deterministic modelling was adopted by Refs. [58–61] to study the combined effect of surface patterns and roughness under hydrodynamic and mixed lubrication by solving the averaged Reynolds equation using the Patir and Cheng approach considering mass-conserving cavitation. Surface roughness was modelled on the micro-scale through stochastic models, while surface patterning was deterministically implemented through proper mesh discretization.

Considering the enormous potential of numerical approaches to boost the design of surface patterns in engineering applications, the aim of this study is to develop and validate a robust numerical approach, which is capable to predict the frictional performance of single- and multi-scale surface patterns applied to journal bearings. For this purpose, beneficial single- and multi-scale patterns have been investigated in mixed-elastohydrodynamic (mixed-EHL) simulations using a multibody simulation (MBS) environment. A crucial aspect is to consider the real surface topography after wearing-in for the individual samples rather than the initial surface topographies. This mixed-EHL simulation approach combined a deterministic asperity contact model with the extended Reynolds equation with flow factors according to Patir/Cheng, which can be further utilized in the design process to optimize the tribological response of engineering systems, e. g. internal combustion engines. The flow factors were obtained through flow simulations on surface pattern scale and the bearing contour was deterministically implemented in the calculation domain. Thereby, Stribeck-like curves were predicted, which allow for the direct comparison with previously determined experimental curves.

## 2. Methods

### 2.1. Workflow

In this study, the speed-dependent frictional performance of journal bearings with single- and multi-scale surface patterns operating in mixed friction under steady load and temperature has been investigated. In these mixed-EHL simulations, the topography, i.e. roughness, surface patterns and bearing contour, has been considered as boundary conditions. The measured bearing contour has been deterministically implemented in the mixed-EHL simulations. In contrast, the influence of roughness and surface patterns has been considered through stochastic models, i.e. flow factors obtained from flow-simulations and asperity contact modelling on the microscopic scale.

### 2.2. Mixed-EHL simulations

Isothermal EHL-simulation in AVL Excite PowerUnit (AVL List GmbH, Graz, Austria) were performed. The aim was to elucidate the impact of single- and multi-scale surface patterns on the frictional performance of journal bearing systems. AVL Excite is a widely used simulation tool for MBS with flexible bodies coupled with detailed investigations on journal bearings. In terms of journal bearing simulations, AVL Excite has successfully demonstrated its capabilities in the simulation of the effects of bearing contour [62,63], roughness [64,65], bearing wear [66], and the consideration of surface patterns [67]. In AVL Excite PowerUnit, the interface between the shaft and the journal bearing can be discretized in circumferential (97 nodes) and axial direction (21 nodes), respectively thus resulting in a total number of 2037 nodes. The general simulation procedure of AVL Excite PowerUnit involves the partitioning of the external load in contributions of the local hydrodynamic and asperity contact pressure (mixed-EHL) as shown in Eq. (1).

$$p_{Total} = p + p_a \quad \text{Eq. 1}$$

The hydrodynamic pressure distribution across the bearing interface is determined by solving the averaged Reynolds equation using a finite volume approach (Eq. (2)). The averaged Reynolds equation includes the effect of surface roughness on the oil flow by the addition of pressure and shear flow factors following the approach of Patir and Cheng [48,49]. The flow factors were numerically determined in flow simulations on the measured surface patches as described in Ref. [68]. Furthermore, the Reynolds equation has been modified by substituting the nominal gap height $h$ by an average gap height $\overline{h}$ according to Wu und Zheng [69]. For the general procedure of the flow factor determination, we refer to Refs. [68,70]. By numerically solving the averaged Reynolds equation, a local lubricant gap height $h$ and hydrodynamic pressure $p$ can be calculated for each node and simulation time-step ($x$,$y$ and $t$). The oil viscosity $\eta$ as well as the sliding speeds of the shaft ($u_1$) and the bearing ($u_2$) are necessary input values. The averaged Reynolds equation has been extended by the mass-conserving cavitation algorithm by Jacobson-Floberg-Olsson (JFO) [71]. Therefore, the fill ratio $\theta$ has been added to prevent pressure build-up in cavitation regions of the bearing.

$$\frac{\partial}{\partial x}\left(\theta\varphi_{p,x}\frac{h^3}{12\eta}\frac{\partial p}{\partial x}\right) - \frac{\partial}{\partial y}\left(\theta\varphi_{p,y}\frac{h^3}{12\eta}\frac{\partial p}{\partial y}\right) + \frac{\partial}{\partial x}\left(\theta\overline{h}\frac{u_1+u_2}{2}\right) + \frac{\partial}{\partial x}\left(\theta\varphi_s\frac{u_1-u_2}{2}\sigma_s\right) + \frac{\partial(\theta\overline{h})}{\partial t} = 0 \quad \text{Eq. 2}$$

For the calculation of the mean asperity contact pressure as a function of the gap height $h$, the approach according to Herbst [34] has been chosen. In this study, an asperity peak has been defined as a point higher than its eight surrounding neighbors referred to as 8P+1 [72] or 9 PP-3D [73]. The radii have been determined via curve fitting over the eight nearest neighbors. For more detailed information on the numerical procedure, interested readers are referred to Refs. [72,73]. Using this approach, the mean asperity contact pressure $p_a(h)$ and the real area of contact $A_a(h)$ can be obtained in dependence of nominal gap height $h$.

$$p_a(h) = \eta_s \int_{z_s=h}^{\infty} P_f(z_s - h)\phi_s(z_s)dz_s \quad \text{Eq. 3}$$

$$A_a(h) = \eta_s A \int_{z_s=h}^{\infty} A_f(z_s - h)\phi_s(z_s)dz_s \quad \text{Eq. 4}$$

Here, $\phi_s(z_s)$ denotes the density distribution of all summit heights. Due to the eccentricity of the bearing, a local mean asperity contact pressure has been obtained at each node.

In the numerical simulation, boundary and operating conditions, i.e. the rheological properties of the PAO oil and the simulation parameters are listed in Table 1. These conditions have been chosen in accordance to the previous experiments [36].

A stationary boundary COF of 0.15 has been chosen based upon previous experiments conducted on a block-on-ring tribometer (Falex Block-on-Ring) under boundary lubrication with a similar material-lubricant combination. The material-pairing and the temporal evolution of the COF are exemplarily shown in Fig. 1.

The measured COF has been added as a parameter (μ) to the mixed-EHL simulation. The local asperity shear stress on the bearing shell (Eq. (4)) is the product of μ and the mean asperity contact pressure (Eq. (3)).

$$\tau_a = -p_a \cdot \mu \quad \text{Eq. 5}$$

Furthermore, the viscous shear stress caused by the lubricant under

**Table 1**
Summary of the oil properties and simulation parameters.

| Lubricant | PAO 4 |
|---|---|
| Kinematic viscosity (40 °C)/mm$^2$·s$^{-1}$ | 16.8 |
| Kinematic viscosity (100 °C)/mm$^2$·s$^{-1}$ | 3.9 |
| **Simulation parameters** | |
| Bearing diameter/mm | 25 |
| Bearing width/mm | 20 |
| Bearing temperature/°C | 40 |
| Oil inlet pressure/bar | 3 |
| Stationary pressure/N·mm$^{-2}$ | 1 |
| Radial load/N | 450 |
| Rotational speed/rpm | 50–600 |
| Linear speed/m·s$^{-1}$ | 0.066 - 0.785 |
| Relative clearance/‰ | 1.4 |

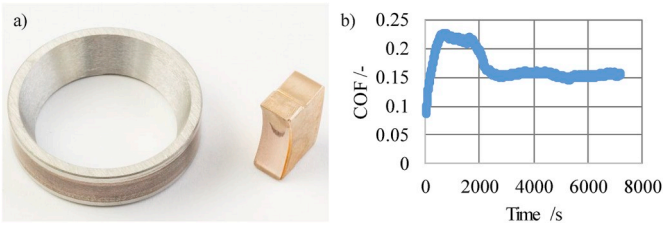


**Fig. 1.** (a) Block-on-ring specimen and (b) the respective COF measurement over time. After having passed the initial running/wearing-in, a steady-state COF of about 0.15 can be observed.

**Table 2**
Surface roughness parameters measured after burnishing using a tactile measuring device.

| Sample | $R_a$/µm | | | $R_q$/µm | | | $R_z$/µm | | |
|---|---|---|---|---|---|---|---|---|---|
| Reference (REF) | 0.16 | ± | 0.02 | 0.20 | ± | 0.02 | 1.07 | ± | 0.09 |

mixed lubrication is calculated according to Eq. (6). The indices $i = 1,2$ refer to the journal and to the bearing shell, respectively.

$$\tau_h = \theta \left\{ \begin{array}{c} \eta \frac{(u_2 - u_1)}{h} (\varphi_f + \varphi_{fs}) + \varphi_{fp} \frac{h}{2} \left( \frac{\partial p}{\partial x} \right) \\ -\frac{\sigma_i}{\sigma} \left( (\varphi_{fp} h - \bar{h}_T) \left( \frac{\partial p}{\partial x} \right) dx - 2\eta \frac{u_2 - u_1}{h} \varphi_{fs} dx \right) \end{array} \right\} \quad \text{Eq. 6}$$

In the following step, both viscous and asperity shear stress are integrated over the bearing surface to calculate the total friction force of the bearing.

$$F_f = \int_A \int (\tau_h + \tau_a)\, dA \quad \text{Eq. 7}$$

The latter can be used to calculate the bearing coefficient of friction (COF) using the bearing radial load ($F_R$).

$$COF = \frac{F_f}{F_R} \quad \text{Eq. 8}$$

### 2.3. Analysis of the surface topography

#### 2.3.1. Bearing contour measurement

The worn bearing contour was measured in ten equally distributed positions across the bearing width utilizing a form tester (MarForm MMQ 100 with probe T2W Mahr). Thereby, the worn contour can be used as an input for the numerical simulation.

#### 2.3.2. Pre-processing of bearing and shaft sleeve topography

The topographies of the bearings and shaft sleeves were measured using white light interferometry WLI (New View 7300, Zygo). For each specimen, three measurements at randomly selected positions in the load area were conducted to consider potential deviations. The surface parameters of the burnished reference (REF) shaft sleeve are listed in Table 2.

Some samples of the burnished reference have been modified by direct laser interference patterning (DLIP), micro-coining (MC) and their combination (MULTI).

The structural parameters of the laser-patterned (DLIP) samples and samples with micro-coining (MC and MULTI) are shown in Table 3.

Comparing the reference surface with all patterned surfaces reveals that the involved roughness scales differ by more than 2 orders of magnitude. Therefore, the magnification of the WLI measurements had to be carefully adjusted. In agreement with Bergmann et al. [74], the reference (REF) and laser-patterned (DLIP) samples were imaged with a magnification of 50×. Thereby, each surface patch contained the height-profile in an area of 140 µm × 105 µm with a resolution of 640 × 480 pixels (0.22 µm/pixel) in circumferential and axial direction, respectively. With an average structural depth of 0.64 µm and periodicity of 5.7 µm, a WLI measurement of the laser-patterned shaft sleeve contains about 111 features. For the micro-coined (MC) and multi-scale (MULTI) samples, a magnification of 20× was chosen due to the considerably increased periodicity of the micro-coined pattern. Each surface patch contains 700 µm × 525 µm with a resolution of 640 × 480 pixels (1.10 µm/pixel). With an average structural width of 155.8 µm and periodicity of 553.9 µm, a measurement contains two features. In a first step, high pass filtering was applied to remove surface waviness and curvature with a maximum wavelength of 250 µm. In addition, low pass filtering with a relative minimum wavelength of $(\lambda_{min}/CR) = 2.5$ was applied to remove measurement errors at single points. In this context, $CR$ denotes the lateral resolution of the white light interferometer. The measured data of the reference and laser-patterned samples as well as the corresponding bearing surfaces were directly used for flow-factor and asperity contact pressure calculations. For the purely micro-coined and multi-scale samples further pre-processing was necessary. In order to reach the area density of about 6% for both samples [36], a combined surface was generated by mirroring and stitching of areas with and without patterns. By mirroring the measurement at the edges a sharp transition at the joint can be avoided [75]. Afterwards, the input for flow-factor and asperity contact pressure calculations was extended to 25 features in an area of 2.73 mm × 2.73 mm. In these cases, the bearing surface was also extended to reach a similar edge length, size and resolution.

## 3. Results and discussion

In order to further explore and elucidate the underlying mechanisms for the previously observed and published improvement in the frictional performance of journal bearings induced by multi-scale patterning [36], the journal bearing system was transferred into a mixed-EHL simulation model. For an accurate modeling of the sliding bearing system, the bearing contour and surface patterns were measured and used as boundary conditions. For the bearing systems with single- and multi-scale patterns, multiple simulation runs were performed with varying rotational speed in agreement with the previously used

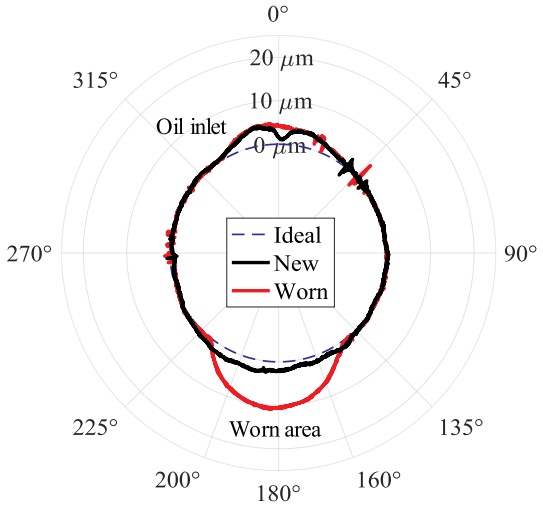


**Fig. 2.** Bearing contour measurements prior to (new) and after the tribological experiments (worn). The oil inlet is located at an angle of 0°, whereas the load area is situated at an angle of 180°.

**Table 3**
Summary of the structural parameters of the patterned samples measured by WLI. Summarized are the structural depth d and width w as well as the periodicity (for multi-scale patterns the periodicity of the primary micro-coined pattern is given).

| Sample | Depth/µm | Width/µm | Periodicity/µm | Area density/% | Aspect ratio (d/w) |
|---|---|---|---|---|---|
| Laser (DLIP) | 0.64 ± 0.2 | 5.8 ± 0.2 | 5.7 ± 0.1 | – | 0.11 |
| Micro-coined (MC) | 35.3 ± 2.1 | 155.2 ± 5.0 | 577.5 ± 24.6 | 5.7 | 0.23 |
| Multi-scale (MULTI) | 35.3 ± 1.3 | 155.8 ± 2.3 | 553.9 ± 18.8 | 6.0 | 0.23 |

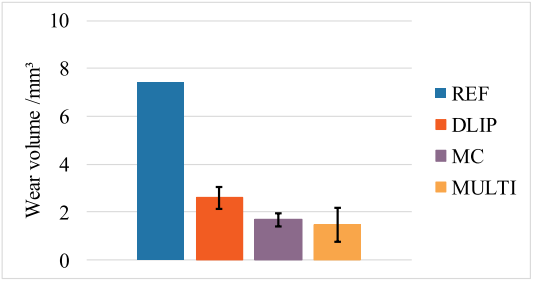


**Fig. 3.** Calculated wear volume based upon bearing contour measurements for all samples.

conditions in the experimental study [36].

### 3.1. Bearing contour wear

Since the underlying lubrication regime can be assigned to mixed lubrication, asperity interactions between the bearing and the shaft lead to wear-induced changes of the bearing contour. Contour lines measured prior to and after the tribological experiments are exemplarily shown in Fig. 2.

Due to stationary loading, the angular expansion of the contour change (wear defect) is limited to the load area (180°). Additionally, the average wear volume $V = \Delta\overline{A}\cdot b$ has been calculated from the average wear area $\Delta\overline{A} = (\sum \Delta A_i)\cdot n^{-1}$ of the individual contour measurements. The individual wear area has been obtained via numerical integration according to equation Eq. (9).

$$\Delta A_i = A_{worn,i} - A_{new,i} = \int_{\gamma}^{\delta}\int_{0}^{r_{worn,i}} r\ dr d\phi - \int_{\gamma}^{\delta}\int_{0}^{r_{new,i}} r\ dr d\phi \qquad \text{Eq. 9}$$

The total wear volume after the experiments (see Ref. [36]) is shown in Fig. 3.

As can be seen in Fig. 3, the highest wear volume is found for the reference bearing without patterning, which fits well with the previously published experimental results [36]. These results demonstrated the highest frictional values for the polished reference sample. All patterned samples lead to a significant reduction of the resulting wear volume, which is in accordance with the reduced COF observed in the mentioned experiments. As outlined in the introduction, surface patterns can differently contribute to improve the corresponding friction and wear performance. Besides a reduction of the real contact area, which may also reduce the asperity interaction, surface patterns help to store wear particles, thus reducing abrasive wear, which is also well reflected in the presented wear analysis.

### 3.2. Surface topography of the shaft sleeve

Fig. 4 shows the initial state of the bearing surface prior to tribological testing. As can be seen in this figure, turning marks in the sliding direction are initially present that potentially originate from the machining process of the bearing bore.

Figs. 5–8 summarize the surface patches of all samples (REF, DLIP, MC and MULTI) measured after the tribological experiments. These surfaces have been used for the contact calculations and flow simulations.

Fig. 5 a and b show that the sleeve topography is subjected to scratches in sliding direction potentially caused by machining and wear

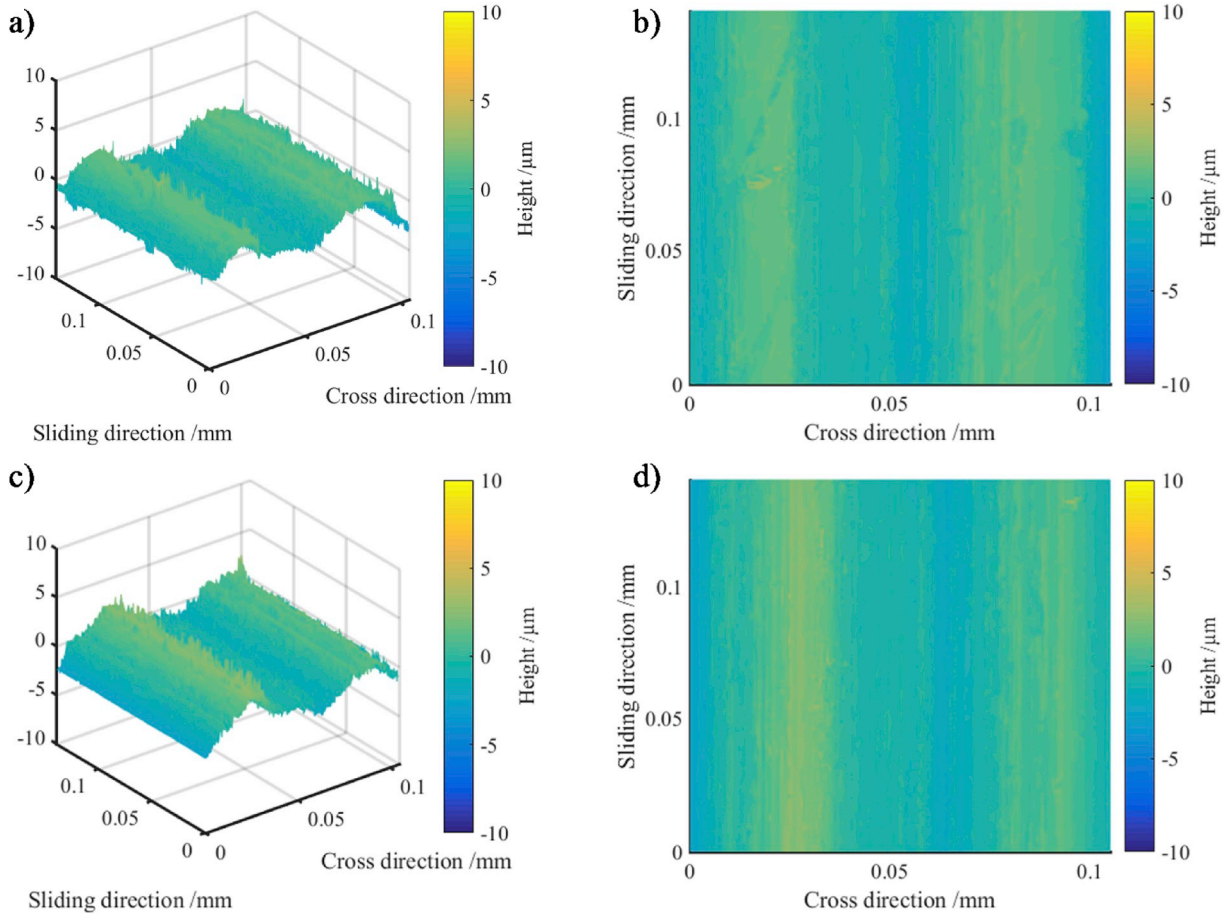


**Fig. 4.** Measured surface topographies (3D and 2D) of the bearing surface at two positions prior to the tribological experiments.

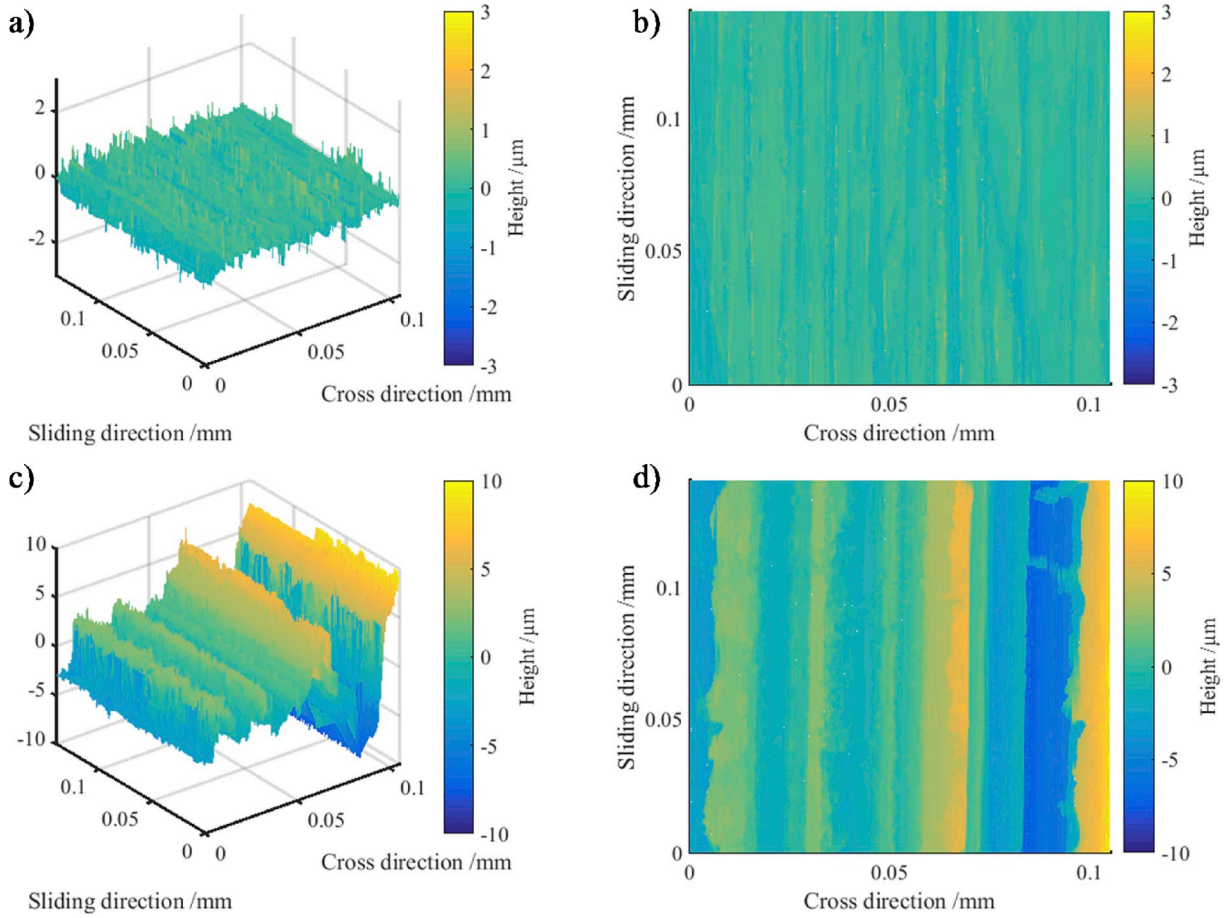


**Fig. 5.** Measured surface topographies (3D and 2D) of the polished reference (REF) of the shaft sleeve (a, b) and the bearing (c, d) after the tribological experiments.

processes. In the reference bearing surface, deep scratches (Fig. 5 c and d) can be observed after the tribological experiment that were not present in the initial state (Fig. 4). Severe interactions between the hard shaft asperities and the softer bearing metal lead to abrasive wear with the removal of abraded material during the process, referred to as micro-cutting [76]. For all combinations with patterned samples (Figs. 6–8), scratches with a significantly reduced depth can be observed, which may suggest a change in the wear mechanism from micro-cutting to micro-ploughing thus resulting in a smoother bearing surface. Additionally, loose wear particles may be trapped in the patterns resulting in reduced three-body-abrasion. An overall reduction of the asperity interactions leading to less wear has been experimentally confirmed, which goes hand in hand with significantly lower frictional losses in DLIP, MC and MULTI systems. For the MC and MULTI systems (Figs. 7 and 8), the periodicity of the scratches appears similar to the periodicity of the dimples of the micro-coining. For the MULTI system (Fig. 8), these scratches are superimposed with DLIP patterns with a lower periodicity.

### 3.3. Flow/shear stress factors and asperity contact pressure curves

To investigate the influence of the different surface topographies in mixed-EHL simulations, their influence on the hydrodynamic and the asperity contact pressure needs to be considered. Therefore, the mean asperity contact pressure $p_a(h)$ as a function of the gap height $h$ (surface separation) was calculated for surface patches from the shaft and the corresponding bearing. Additionally, flow simulations have been performed to derive flow factors according to Patir and Cheng for their incorporation in the Reynolds equation. In order to compare the numerical results to the results from our previous experimental study, the flow factors and asperity contact pressure curves have been calculated from the surfaces that have been measured in the worn-in state after the experiment [36].

As can be seen in Fig. 9 a, the REF and DLIP sample show a generally different behavior than the MC and MULTI sample. For the REF and DLIP sample, the pressure flow factor in sliding direction $\varphi_{p,x}$ is greater than unity for all surface separations. In case of the REF sample, this leads to the conclusion that the deeper scratches with a preferential orientation along the sliding direction as observed in Fig. 6 have a negative influence on the generation of hydrodynamic pressure since they may increase the oil flow out of the contact zone in this direction. Comparing the REF and DLIP sample, the DLIP sample shows similar tendencies but to a lesser extent. This can be traced back to the isotropy of the fabricated pattern on the shaft sleeve which hinders the flow in sliding direction whereas the scratches on the bearing in sliding direction increase the oil flow out of the contact zone. A positive effect in terms of restricted flow conditions thus promoting the generation of hydrodynamic pressure can be observed for the MC and MULTI samples for which the pressure flow factor $\varphi_{p,x}$ demonstrates significantly lower values than 1 up to surface separations of 10 µm. This leads to the conclusion that these surface topographies may notably contribute to an improved load-bearing capacity. As can be seen in Fig. 9 b, all samples investigated show beneficial values in terms of the pressure flow factor in cross-sliding direction $\varphi_{p,y}$. For the REF sample, the best behavior can be observed, which can be directly correlated with the directionality of the surface roughness perpendicular to this direction. In contrast, the patterned samples show a less beneficial behavior, which points to a reduced load-bearing capacity. As can be seen in Fig. 9 b, the smallest load bearing capacity in cross-sliding direction may be expected for the DLIP system. Taking both pressure flow factors $\varphi_{p,x}$ and $\varphi_{p,y}$ into

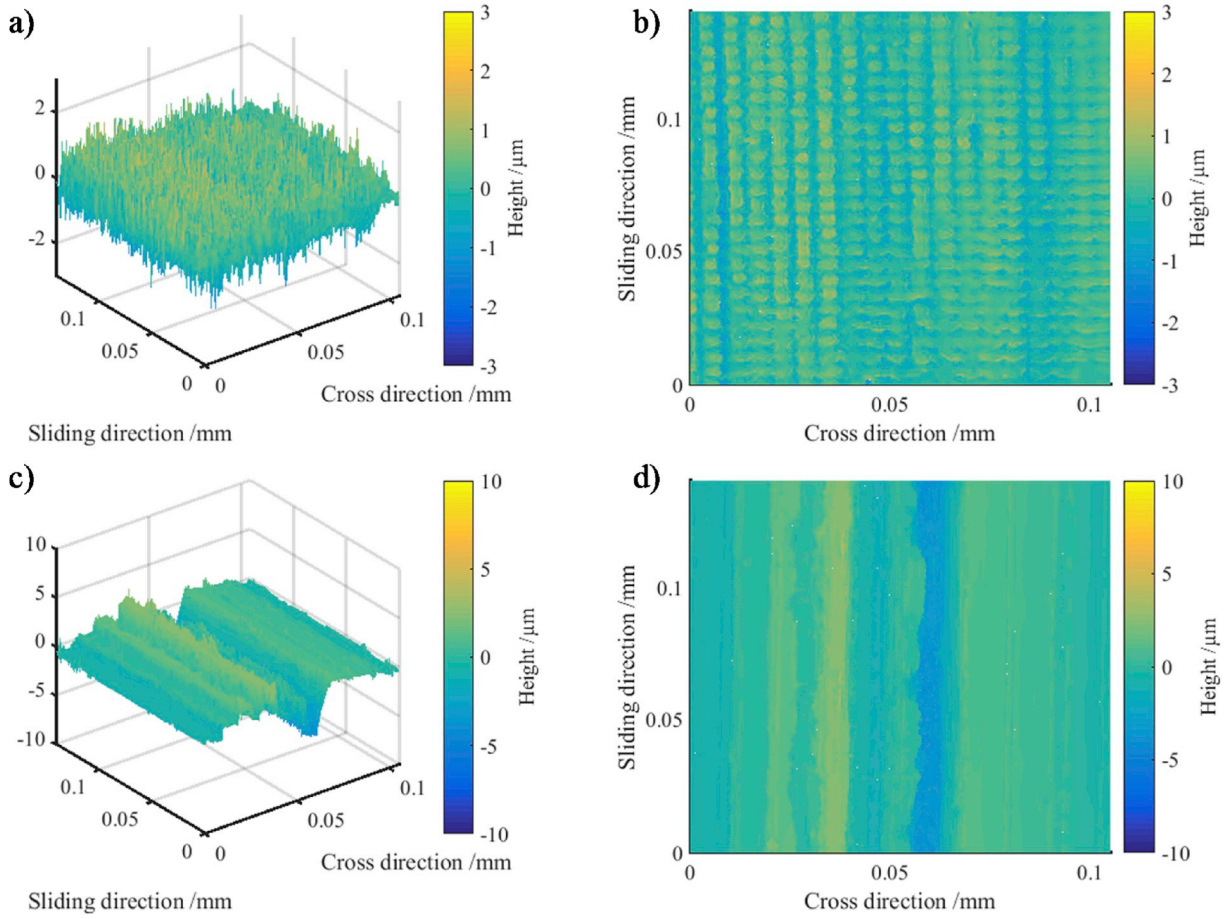


**Fig. 6.** Measured surface topographies (3D and 2D) of the laser-patterned samples (DLIP) of the shaft sleeve (a, b) and the bearing (c, d) after the tribological experiments.

consideration, makes obvious that beneficial effects in terms of restricted fluid flow can be observed for the MC and MULTI samples. This goes hand in hand with the conclusion that the overall behavior may be dominated by the coarser micro-coined surface topography. The consideration of the shear flow factor in sliding direction $\varphi_s$ (Fig. 9 c) points in a similar direction. It becomes obvious that the calculated shear flow for the REF sample is always negative irrespective of the surface separation, thus indicating a decreased flow (less beneficial), which can be traced back to the smoother surface of the moving sleeve surface as well as the severe scratches in sliding direction observed on the bearing surface. In contrast, the DLIP sample shows an increased oil flow with a maximum at a surface separation of around 1 µm, which fits well with the pattern depth of the DLIP sample. Taking the MC and MULTI samples into consideration, these samples show positive values irrespective of the surface separation thus pointing towards an increased overall flow (beneficial behavior). The similar behavior of both samples again indicates that the behavior is mainly dominated by the coarser and deeper micro-coined patterns.

In order to calculate the contribution of viscous friction (Eq. (6).), the shear stress factors according to Patir and Cheng [49] have been considered. In agreement with the approach of Patir and Cheng, the shear stress factor of all samples considered approaches 1 for larger surface separations (Fig. 9 d). For the REF sample, this factor rapidly increases with decreasing surface separation thus reaching a maximum at around 3 µm followed by a subsequent decrease for smaller surface separations. The DLIP sample shows a similar behavior but the curve is shifted to lower surface separations, which again matches well with the involved pattern depth. In contrast, the MC and MULTI sample show an increase without establishing a pronounced plateau value. These results may be connected with the corresponding lubrication conditions, which change as a function of the surface separation. The shear stress factor $\varphi_{fp}$ (correction factor for the mean pressure flow component as displayed in Fig. 9 e) is negligible for REF and DLIP as it is predominantly determined by the longitudinally orientated bearing roughness. For the MC and MULTI samples, a dominant influence on the viscous shear stress can be observed, which is caused by the effective oil-film pressure at low surface separation. For a detailed numerical explanation we refer to Ref. [77]. Similar to the shear flow factor $\varphi_s$, the shear stress factor $\varphi_{fs}$ (Fig. 9 f) results from a combined influence of the pattern and the relative motion. For the REF sample, for which the smoother REF sample is in contact with the rougher bearing surface, the viscous shear stress is significantly enhanced due the effect of the rougher counter-body. For the MC and MULTI samples, the additional flow transport due to the moving micro-coined surface (rougher surfaces) increases the velocity gradient in the film, which leads to decreased shear stress. For the DLIP sample, no significant influence ($\varphi_{fs} = 0$) can be observed at separations above 2 µm. At lower separations, the shear-induced generation of an additional oil flow leads to reduced shear stresses, which again correlates well with the overall roughness scale of the DLIP sample. When the nominal gap height becomes small, the average gap height $\bar{h}$ according to Wu und Zheng [69] differs from the nominal gap height (Fig. 9 g). This effect is visible for all cases and most dominant for the REF case, where wear-induced changes of bearing roughness are most pronounced. This goes hand in hand with the observed trends in the contact factor $\varphi_c$ depicted in Fig. 9 h.

The asperity contact curves are significantly affected by the topography of the counter-body. In this regard, the smooth bearing surface of

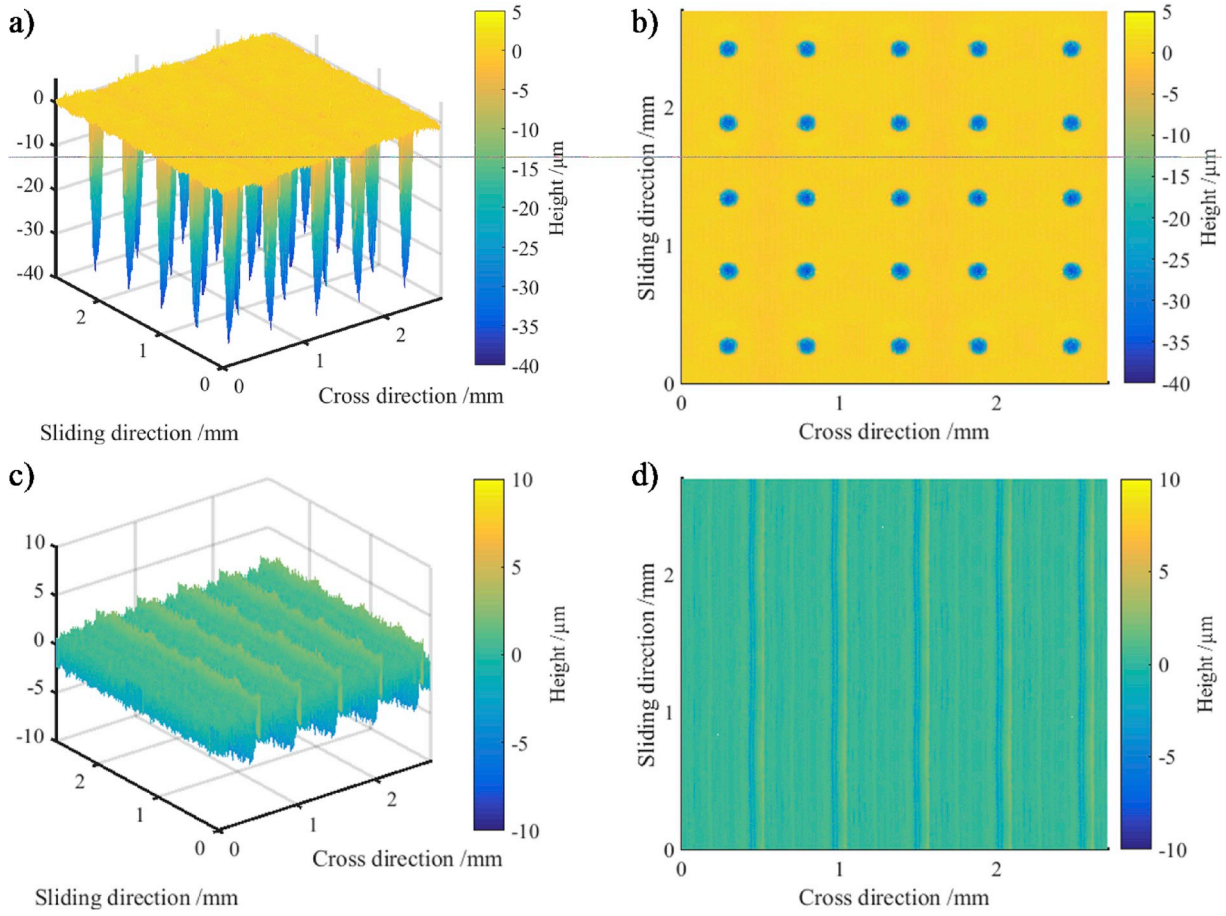


**Fig. 7.** Measured surface topographies (3D and 2D) of the micro-coined samples (MC) of the shaft sleeve (a, b) and the bearing (c, d) after the tribological experiments.

the DLIP sample leads to a transition from hydrodynamic to mixed friction at a nominal gap height of 4 µm. For the rougher bearing surface of the REF, the transition lays at 10 µm. For the MC and MULTI sample, the transition nominal gap height of 5 (MULTI) and 10 µm (MC) of the asperity contact pressure curves are affected by the MC pattern. In these cases, the description of surface separation in terms of the nominal gap height may lead to a misleading interpretation of the asperity contact pressure curves (MC and MULTI in Fig. 9 a). The nominal gap height is defined as the difference between the mean levels of the two rough surfaces [78]. With micro-coined patterns present, the mean level of that surface is moved further from the top asperities, which leads to an arbitrary increase of the nominal gap height. Comparing the asperity contact pressure over nominal gap height for the REF and MC cases, the asperity contact of the REF has a much higher gradient. Thus, small decreases of the nominal gap height lead to high asperity contact pressures thus resulting in severe mixed friction conditions. For the MC sample, the reduction of nominal gap height to a value of 6 µm leads to a slight increase in the asperity contact pressure and hence to less severe conditions compared to the reference sample. This is caused by a significantly higher contact area ratio for the REF sample with decreasing surface separation. Thus, high values of asperity contact pressure are present for large contact areas. As the definition of the nominal gap height is similar for both asperity contact pressure curves as well as flow factors, the hydrodynamic and asperity contact pressure problem is treated in a similar manner.

### 3.4. Simulation of frictional performance

The numerical frictional analysis shows qualitatively similar results compared to the previously published experimental results [36]. Similar to the results from our previous experimental study, the REF shows the highest COF for all speeds (Fig. 11 a). With decreasing speed, the COF increases. It can be calculated that the hydrodynamic pressure for the REF sample is approximately 0.75 MPa at maximum speed (Fig. 11 b). At lower speeds, the hydrodynamic pressure build-up decreases and fully exceeds below 250 1/min as the maximum hydrodynamic pressure equals the supply pressure of the oil feed (0.3 MPa). In contrast, the asperity contact pressure of the REF sample is significantly higher ranging between 35 and 43 MPa (Fig. 11 b and c). Thus, the majority of load is carried by the asperity contact pressure at all speeds.

Compared to the REF, a large improvement of frictional performance can be observed for all patterned systems at all speeds. In agreement with the previous experimental results, low COF values can be observed for speeds above 250 1/min, especially for the DLIP and MULTI sample (Fig. 10 a). This can be traced back to the fact that a large proportion of load is carried by the hydrodynamic (oil-film) pressure ($p_{oil}$) in case of these surface patterns. Notably, the pressure flow factors ($\varphi_{p,x}$ and $\varphi_{p,y}$) of the DLIP sample indicate a negative influence on the load carrying capacity, whereas the MULTI sample's flow factors suggest a positive effect. This clearly demonstrates the system-specific interplay of hydrodynamics and asperity contact pressure in mixed-EHL simulations. Assumptions solely based upon the evaluation of flow factors or asperity contact pressure curves may therefore lead to wrong conclusions. For the samples with laser patterns (DLIP and MULTI), a speed-dependent local maxima hydrodynamic pressure at 350 1/min (DLIP) and 450 1/min (MULTI) can be observed indicating the favorable operating point of these systems. For the micro-coined (MC) sample, the hydrodynamic pressure decreases with decreasing speed. Thus, the favorable operating

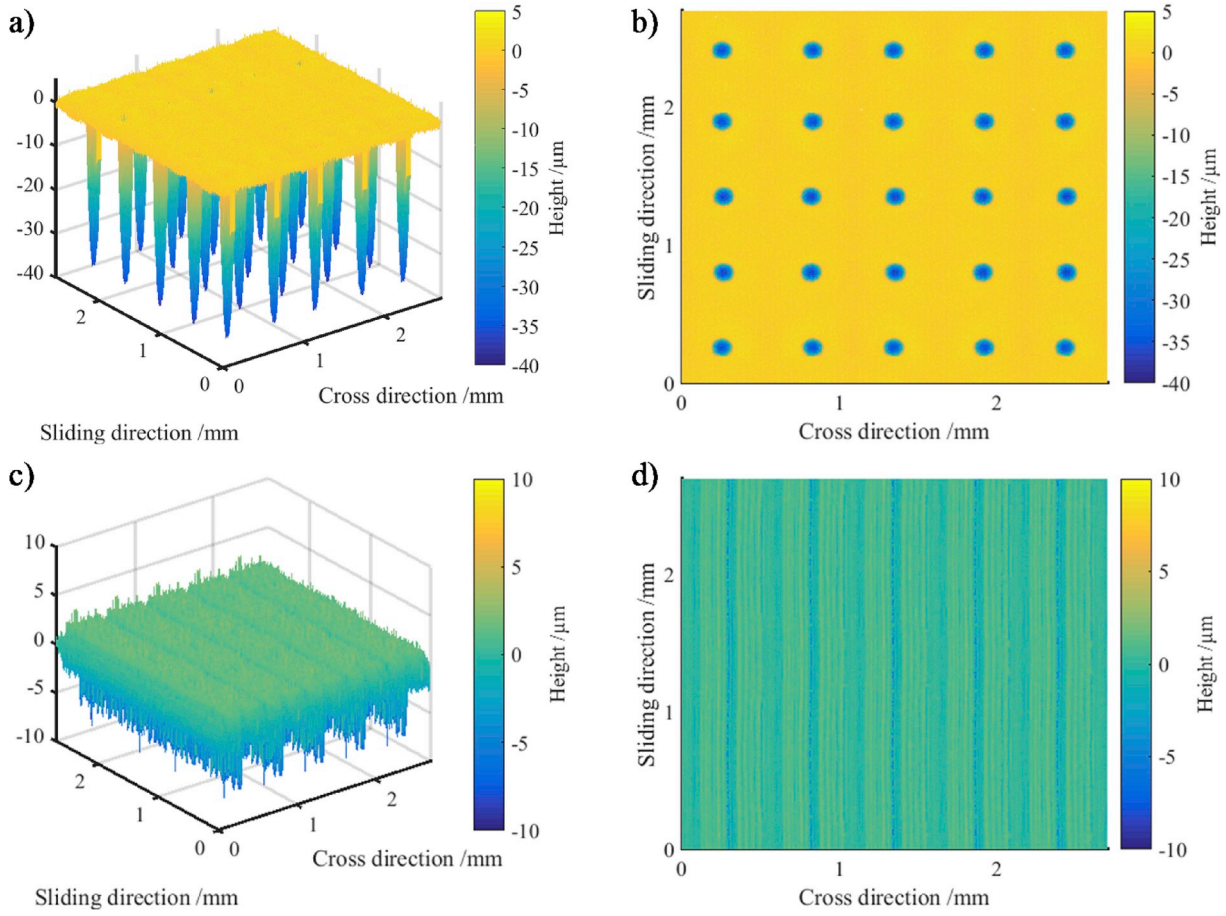


**Fig. 8.** Measured surface topographies (3D and 2D) of the multi-scale sample (MULTI) of the shaft sleeve (a, b) and the bearing (c, d) after the tribological experiments.

point would appear at higher rotational speeds than considered in this study (Fig. 11 b). At lower speeds, the onset of asperity contact pressure leads to an increase of the estimated COF for the DLIP and MULTI samples. However, the frictional performance at lower speeds is still better compared to the REF, which can be explained by two beneficial effects induced by the surface patterns. First, the build-up of the hydrodynamic pressure is notably improved as can be figured from the flow factors used in the Reynold's equation (Eq. (2)). Moreover, the DLIP and MULTI samples show a reduced asperity contact pressure at lower rotational speeds. As the speed gradually decreases, lower absolute values of asperity contact pressure are still present for all patterned surfaces (see Fig. 11 c). The minimum nominal gap heights of the REF and DLIP samples are significantly influenced by the bearing surface roughness, as can be seen in Fig. 11 d. Using DLIP, the nominal gap height can significantly be reduced, which demonstrates the improved wearing-in under severe operating conditions. The nominal gap heights of the MULTI and MC samples lay between the respective values of the REF and DLIP samples (Fig. 11 d).

### 3.5. Validation of the numerical method

Comparing the numerical results to the experimental study [36], good agreement for the frictional behavior can be observed. Similar to the simulation results, the REF sample operates under mixed friction conditions for all speeds. The largest deviation is present at 600 1/min for which the simulation predicts a COF of about 0.15 compared to the experimentally measured value of 0.12, which still lays in an acceptable interval. At lower speeds, an even better quantitative agreement between simulation and experiments has been achieved. For the DLIP sample, low and constant COF values have been measured at rotational speeds above 300 1/min, which agrees with the presented simulation results. Furthermore, the simulated rise of COF at rotational speeds below 300 1/min is qualitatively and quantitatively consistent with the experimental trends. In the previous experimental study, maximum friction reduction has been observed for the MULTI sample, whereas in the present simulation the DLIP sample showed a slightly better frictional performance for all rotational speeds. A larger deviation between experiment and simulation can be observed for the MC sample. In the experimental study, the MC sample showed a Stribeck-like behavior with low frictional losses at rotational speeds above 300 1/min. In contrary, the COF rises continuously with decreasing speed in the numerical study (Fig. 11 a). The distinct difference in the simulated asperity contact pressure is responsible for the differences in COF as the asperity contact pressure curve for the MC sample shows an onset of asperity contact for larger surface separations. In contrast, the flow factors obtained for the MC and MULTI samples are rather similar. Despite this deviation, it must be emphasized, that the general ranking of frictional performance of the MC sample is similar. A further potential cause for the deviations in the frictional behavior of the micro-coined samples (MC and MULTI) is the average flow model by Patir and Cheng. Using the pressure and shear flow factors following the approach of Patir and Cheng, the nominal gap height is introduced into the Reynolds equation, which is strongly affected by the MC pattern. This uncertainty could be obliterated with different averaging techniques of the Reynolds equation, i.e. homogenization technique [70,79,80], for which the actual gap height is considered. Instead of using the nominal gap height, which is defined as the distance between the centerlines of two rough surfaces, the description, homogenization factors, asperity

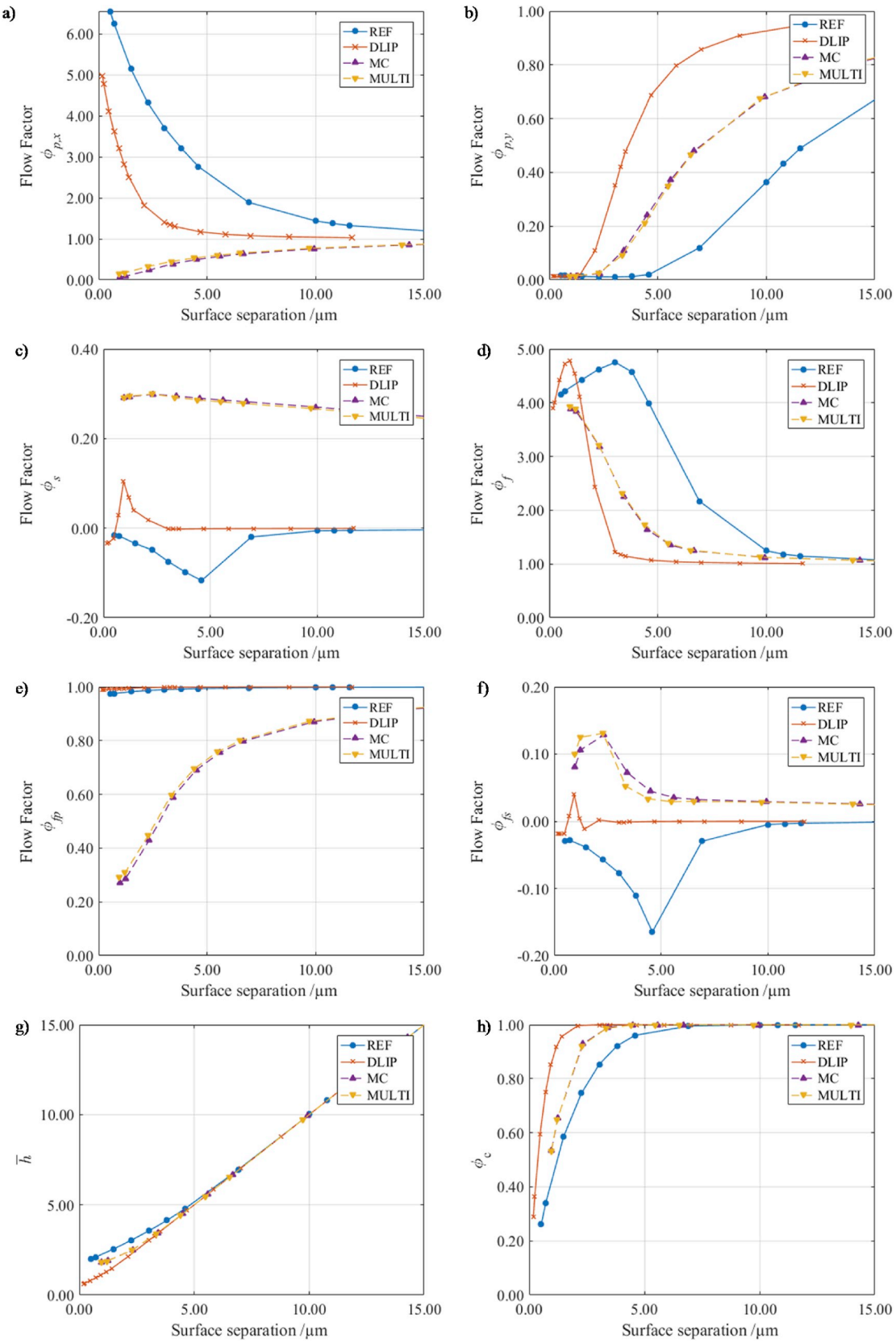


**Fig. 9.** Flow factors for the bearing systems: (a) Pressure flow factor in sliding direction $\varphi_{p,x}$. (b) Pressure flow factor in cross-sliding direction $\varphi_{p,y}$. (c) Shear flow factor in sliding direction $\varphi_s$. (d) Shear stress factor in sliding direction $\varphi_f$. (e) Shear stress factor $\varphi_{fp}$. (f) Shear stress factor in cross-sliding direction $\varphi_{fs}$. (g) Correlation between average gap height $\overline{h}$ and surface separation h. (h) Contact factor $\varphi_c$. These factors describe the influence of the patterns and roughness on the hydrodynamic pressure in the Reynolds equation and the computed viscous-friction losses (please refer to section 2).

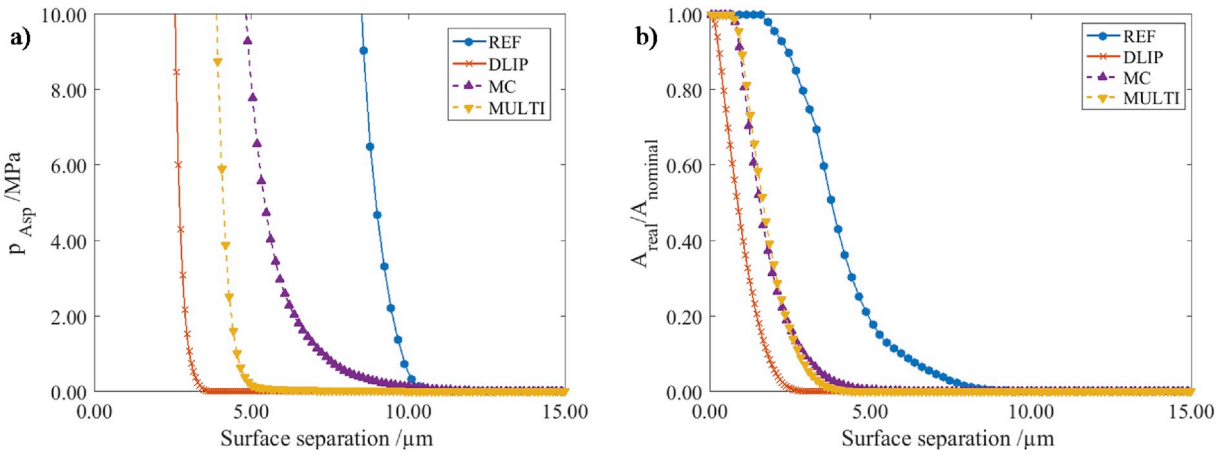


**Fig. 10.** (a) Asperity contact pressure curves for all samples studied. The intersection of the contact pressure curves with the x-axis indicates the nominal transition gap height from hydrodynamic to mixed lubrication. (b) Contact area ratio shows the ratio between the real and the nominal contact area of the asperity contact. In this context, mixed-friction conditions can be calculated with the load sharing concept introduced in section 2.

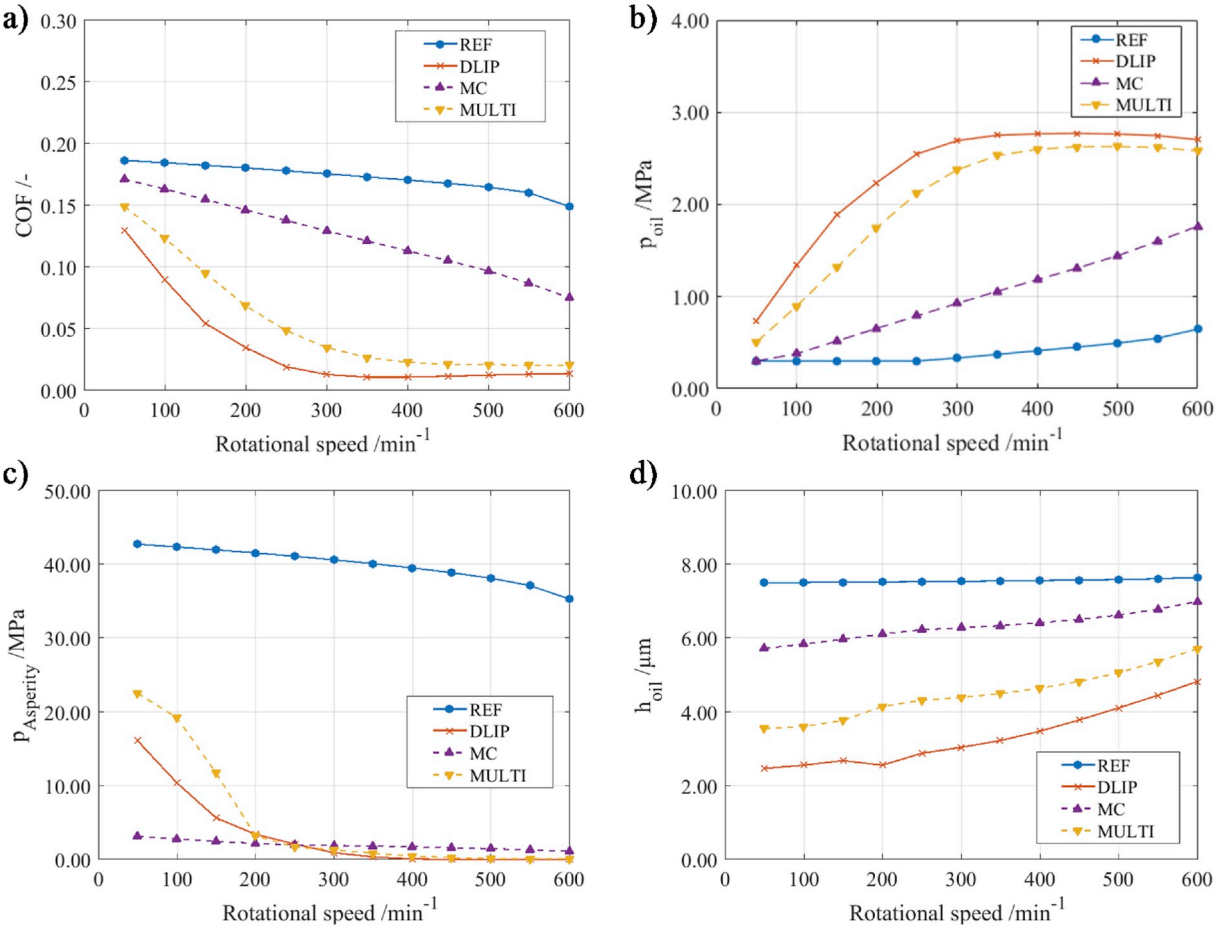


**Fig. 11.** Summary of the results of the mixed-EHL simulation for all samples studied: (a) COF, (b) local, maximum oil pressure, (c) local, maximum asperity contact pressure, (d) minimal oil film thickness (minimal gap height).

contact pressure curves (Fig. 10 a) and the resulting gap height (Fig. 11 d) can be evaluated over the actual gap height. This could improve the mutual understanding of single-scale and multi-scale surface patterns. In the design process of single- and multi-scale surface patterns for journal bearings subjected to mixed lubrication, further effects have to be taken into account such as wear-induced changes of the bearing contour and the surface topography. This can affect the load carrying capacity and the rotational speeds for the transition from mixed to full lubrication under steady load [66]. Furthermore, with decreasing gap heights under severe mixed-lubricated conditions, the actual positioning of asperity tips and grooves should be taken into account by methods such as relocation technique as introduced by Furustig et al. [81]. Thereby, the actual, local conformity ("familiarity factor") of the sliding surfaces is considered when determining the asperity contact pressure curves and

real contact area of systems with patterned surfaces.

## 4. Conclusions

To pave the way for journal bearings with single and multi-scale surface patterns into industrial applications, their frictional performance has been investigated in mixed-elastohydrodynamic (mixed-EHL) simulations using a multi-body simulation (MBS) environment. Therefore, the topography of the shaft sleeve with single- and multi-scale surface patterns has been used as input parameters in a mixed-EHL simulation combining a deterministic asperity contact model and extended Reynolds equation with Patir/Cheng flow factors. Based upon the results obtained, the following conclusions can be drawn:

1. Bearing wear can be significantly reduced with patterned shaft surfaces since the onset of mixed lubrication and thus higher wear is shifted to lower rotational speeds. The maximum wear reduction of 80% compared to the unpatterned shaft sleeves (REF) was achieved for the multi-scale patterns (MULTI). Micro-coined and laser-patterned single-scale features induced a wear reduction of 78% and 65%, respectively.
2. Single- and multi-scale patterns induced a shift in the transition from mixed to hydrodynamic lubrication to smaller rotational speeds with notably reduced COFs. According to our simulation results, the COF is most significantly reduced by laser patterning (DLIP) followed by multi-scale patterning (MULTI) and micro-coining (MC). The simulation verified that the build-up of hydrodynamic pressure is promoted, whereas asperity contact pressure is reduced for single- and multi-scale surface patterns.
3. Asperity contact pressure is reduced as a consequence of smoother bearing surfaces for single- and multi-scale patterns. For the reference sample, severe scratches on the bearing surface led to the occurrence of mixed lubrication even at large nominal gap heights. Using DLIP, the nominal gap height can be significantly reduced, which demonstrates the improved wearing-in under severe operating conditions.

## Declaration of competing interest

The authors declare that they have no known competing financial interests or personal relationships that could have appeared to influence the work reported in this paper.

## Acknowledgements

The present work is supported by funding from the Deutsche Forschungsgemeinschaft (DFG, projects: MU 959/27-2 and HI 790/33-2 within the SPP 1551). A. Rosenkranz gratefully acknowledges the financial support given by CONICYT in the project FONDECYT 11180121. In addition, A. Rosenkranz would like to acknowledge the financial support given by the VID in the framework of U-Inicia UI 013/2018 as well as the academic direction of the University of Chile. F. König and G. Jacobs gratefully acknowledge the DFG for the funding of the graduate school GRK 1856, Integrated Energy Supply Modules for Roadbound E-Mobility". Furthermore, F. König acknowledges Dres. Emmanuel Georgiou and Dirk Drees from Falex Tribology NV for their valuable contributions.

## References

[1] Etsion I, Kligerman Y, Halperin G. Analytical and experimental investigation of laser-textured mechanical seal faces. Tribol Trans 1999;42(3):511–6. https://doi.org/10.1080/10402009908982248.
[2] Etsion I. State of the art in laser surface texturing. J Tribol 2005;127(1):248. https://doi.org/10.1115/1.1828070.
[3] Hsu SM, Jing Y, Hua D, Zhang H. Friction reduction using discrete surface textures: principle and design. J Phys D: Appl Phys 2014;47(33):335307. https://doi.org/10.1088/0022-3727/47/33/335307.
[4] Gropper D, Wang L, Harvey TJ. Hydrodynamic lubrication of textured surfaces: a review of modeling techniques and key findings. Tribol Int 2016;94:509–29. https://doi.org/10.1016/j.triboint.2015.10.009.
[5] Gachot C, Rosenkranz A, Reinert L, Ramos-Moore E, Souza N, Müser MH, et al. Dry friction between laser-patterned surfaces: role of alignment, structural wavelength and surface chemistry. Tribol Lett 2013;49(1):193–202. https://doi.org/10.1007/s11249-012-0057-y.
[6] Prodanov N, Gachot C, Rosenkranz A, Mücklich F, Müser MH. Contact mechanics of laser-textured surfaces. Tribol Lett 2013;50(1):41–8. https://doi.org/10.1007/s11249-012-0064-z.
[7] Borghi A, Gualtieri E, Marchetto D, Moretti L, Valeri S. Tribological effects of surface texturing on nitriding steel for high-performance engine applications. Wear 2008;265(7–8):1046–51. https://doi.org/10.1016/j.wear.2008.02.011.
[8] Pettersson U, Jacobson S. Influence of surface texture on boundary lubricated sliding contacts. Tribol Int 2003;36(11):857–64. https://doi.org/10.1016/S0301-679X(03)00104-X.
[9] Grabon W, Koszela W, Pawlus P, Ochwat S. Improving tribological behaviour of piston ring–cylinder liner frictional pair by liner surface texturing. Tribol Int 2013;61:102–8. https://doi.org/10.1016/j.triboint.2012.11.027.
[10] zum Gahr K-H, Wahl R, Wauthier K. Experimental study of the effect of microtexturing on oil lubricated ceramic/steel friction pairs. Wear 2009;267(5–8):1241–51. https://doi.org/10.1016/j.wear.2008.12.108.
[11] Rosenkranz A, Heib T, Gachot C, Mücklich F. Oil film lifetime and wear particle analysis of laser-patterned stainless steel surfaces. Wear 2015;334–335:1–12. https://doi.org/10.1016/j.wear.2015.04.006.
[12] Andersson P, Koskinen J, Varjus S, Gerbig Y, Haefke H, Georgiou S, et al. Microlubrication effect by laser-textured steel surfaces. Wear 2007;262(3):369–79. https://doi.org/10.1016/j.wear.2006.06.003.
[13] Fowell MT, Medina S, Olver AV, Spikes HA, Pegg IG. Parametric study of texturing in convergent bearings. Tribol Int 2012;52:7–16. https://doi.org/10.1016/j.triboint.2012.02.013.
[14] Fowell M, Olver AV, Gosman AD, Spikes HA, Pegg I. Entrainment and inlet suction: two mechanisms of hydrodynamic lubrication in textured bearings. Tribol Trans 2007;129(2):336. https://doi.org/10.1115/1.2540089.
[15] Braun D, Greiner C, Schneider J, Gumbsch P. Efficiency of laser surface texturing in the reduction of friction under mixed lubrication. Tribol Int 2014;77:142–7. https://doi.org/10.1016/j.triboint.2014.04.012.
[16] Costa HL, Hutchings IM. Hydrodynamic lubrication of textured steel surfaces under reciprocating sliding conditions. Tribol Int 2007;40(8):1227–38. https://doi.org/10.1016/j.triboint.2007.01.014.
[17] Rosenkranz A, Costa HL, Profito F, Gachot C, Medina S, Dini D. Influence of surface texturing on hydrodynamic friction in plane converging bearings - an experimental and numerical approach. Tribol Int 2019;134:190–204. https://doi.org/10.1016/j.triboint.2019.01.042.
[18] Tala-Ighil N, Fillon M, Maspeyrot P. Effect of textured area on the performances of a hydrodynamic journal bearing. Tribol Int 2011;44(3):211–9. https://doi.org/10.1016/j.triboint.2010.10.003.
[19] Gachot C, Hsu C, Suárez S, Grützmacher P, Rosenkranz A, Stratmann A, et al. Microstructural and chemical characterization of the tribolayer formation in highly loaded cylindrical roller thrust bearings. Lubricants 2016;4(2):19. https://doi.org/10.3390/lubricants4020019.
[20] Hsu C-J, Stratmann A, Rosenkranz A, Gachot C. Enhanced growth of ZDDP-based tribofilms on laser-interference patterned cylinder roller bearings. Lubricants 2017;5(4):39. https://doi.org/10.3390/lubricants5040039.
[21] Gachot C, Rosenkranz A, Hsu SM, Costa HL. A critical assessment of surface texturing for friction and wear improvement. Wear 2017;372–373:21–41. https://doi.org/10.1016/j.wear.2016.11.020.
[22] Rosenkranz A, Grützmacher PG, Gachot C, Costa HL. Surface texturing in machine elements – a critical discussion for rolling and sliding contacts. Adv Eng Mater 2019;86:1900194. https://doi.org/10.1002/adem.201900194.
[23] Jiang L, Zhao Y, Zhai J. A lotus-leaf-like superhydrophobic surface: a porous microsphere/nanofiber composite film prepared by electrohydrodynamics. Angew Chem Int Ed Engl 2004;43(33):4338–41. https://doi.org/10.1002/anie.200460333.
[24] Koch K, Bhushan B, Jung YC, Barthlott W. Fabrication of artificial Lotus leaves and significance of hierarchical structure for superhydrophobicity and low adhesion. Soft Matter 2009;5(7):1386. https://doi.org/10.1039/b818940d.
[25] Gao H, Wang X, Yao H, Gorb S, Arzt E. Mechanics of hierarchical adhesion structures of geckos. Mech Mater 2005;37(2):275–85. https://doi.org/10.1016/j.mechmat.2004.03.008.
[26] Greiner C, Arzt E, del Campo A. Hierarchical gecko-like adhesives. Adv Mater 2009;21(4):479–82. https://doi.org/10.1002/adma.200801548.
[27] Zheng Y, Gao X, Jiang L. Directional adhesion of superhydrophobic butterfly wings. Soft Matter 2007;3(2):178–82. https://doi.org/10.1039/B612667G.
[28] Tan Y, Gu J, Zang X, Xu W, Shi K, Xu L, et al. Versatile fabrication of intact three-dimensional metallic butterfly wing scales with hierarchical sub-micrometer structures. Angew Chem Int Ed Engl 2011;50(36):8307–11. https://doi.org/10.1002/anie.201103505.
[29] Bixler GD, Bhushan B. Fluid drag reduction with shark-skin riblet inspired microstructured surfaces. Adv Funct Mater 2013;23(36):4507–28. https://doi.org/10.1002/adfm.201203683.

[30] Dean B, Bhushan B. Shark-skin surfaces for fluid-drag reduction in turbulent flow: a review. Philos Trans A Math Phys Eng Sci 2010;368(1929):4775–806. https://doi.org/10.1098/rsta.2010.0201.

[31] Nosonovsky M. Multiscale roughness and stability of superhydrophobic biomimetic interfaces. Langmuir 2007;23(6):3157–61. https://doi.org/10.1021/la062301d.

[32] Hsu SM, Jing Y, Zhao F. Self-adaptive surface texture design for friction reduction across the lubrication regimes. Surf Topogr: Metrol Prop 2016;4(1):14004. https://doi.org/10.1088/2051-672X/4/1/014004.

[33] Resendiz J, Egberts P, Park SS. Tribological behavior of multi-scaled patterned surfaces machined through inclined end milling and micro shot blasting. Tribol Lett 2018;66(4):750. https://doi.org/10.1007/s11249-018-1086-y.

[34] Wang X, Adachi K, Otsuka K, Kato K. Optimization of the surface texture for silicon carbide sliding in water. Appl Surf Sci 2006;253(3):1282–6. https://doi.org/10.1016/j.apsusc.2006.01.076.

[35] Grützmacher PG, Rosenkranz A, Szurdak A, Gachot C, Hirt G, Mücklich F. Effects of multi-scale patterning on the run-in behavior of steel-alumina pairings under lubricated conditions. Adv Eng Mater 2018;20(1):1700521. https://doi.org/10.1002/adem.201700521.

[36] Grützmacher PG, Rosenkranz A, Szurdak A, König F, Jacobs G, Hirt G, et al. From lab to application - improved frictional performance of journal bearings induced by single- and multi-scale surface patterns. Tribol Int 2018;127:500–8. https://doi.org/10.1016/j.triboint.2018.06.036.

[37] Rosenkranz A, Grützmacher PG, Murzyn K, Mathieu C, Mücklich F. Multi-scale surface patterning to tune friction under mixed lubricated conditions. Appl Nanosci 2019;262:369. https://doi.org/10.1007/s13204-019-01055-9.

[38] Rom M, Müller S. An effective Navier-Stokes model for the simulation of textured surface lubrication. Tribol Int 2018;124:247–58. https://doi.org/10.1016/j.triboint.2018.04.011.

[39] Rom M, Müller S. A new model for textured surface lubrication based on a modified Reynolds equation including inertia effects. Tribol Int 2019;133:55–66. https://doi.org/10.1016/j.triboint.2018.12.030.

[40] Keller D, Jacobs G, Kramer A, Neumann S, Paulkowski D, Eifel S. Friction reduction of dynamic elastomer seals by microstructuring of the seal sliding surface. In: Zylinderlaufbahn, Kolben, Pleuel 2018 der Kurbeltrieb im Spannungsfeld unterschiedlicher Anforderungen Baden Baden, 05. und 06. Juni 2018. VDI-Fachtagung/VDI-Gesellschaft Materials Engineering. Düsseldorf: VDI Verlag GmbH; 2018. p. 137–52.

[41] Hu Y-Z, Zhu D. A full numerical solution to the mixed lubrication in point contacts. Wear 2000;122(1):1. https://doi.org/10.1115/1.555322.

[42] Ren N, Zhu D, Chen WW, Liu Y, Wang QJ. A three-dimensional deterministic model for rough surface line-contact EHL problems. J Tribol 2009;131(1):11501. https://doi.org/10.1115/1.2991291.

[43] Zhu D, Hu Y-Z. A computer program package for the prediction of EHL and mixed lubrication characteristics, friction, subsurface stresses and flash temperatures based on measured 3-D surface roughness. Tribol Trans 2001;44(3):383–90. https://doi.org/10.1080/10402000108982471.

[44] Zhu D, Hu Y-Z. Effects of rough surface topography and orientation on the characteristics of EHD and mixed lubrication in both circular and elliptical contacts. Tribol Trans 2001;44(3):391–8. https://doi.org/10.1080/10402000108982472.

[45] Zhu D, Jane Wang Q. Elastohydrodynamic lubrication: a gateway to interfacial mechanics—review and prospect. J Tribol 2011;133(4):41001. https://doi.org/10.1115/1.4004457.

[46] Wang QJ, Zhu D. Virtual texturing: modeling the performance of lubricated contacts of engineered surfaces. J Tribol 2005;127(4):722. https://doi.org/10.1115/1.2000273.

[47] Zhu D, Nanbu T, Ren N, Yasuda Y, Wang QJ. Model-based virtual surface texturing for concentrated conformal-contact lubrication. Proc Inst Mech Eng J J Eng Tribol 2010;224(8):685–96. https://doi.org/10.1243/13506501JET739.

[48] Patir N, Cheng HS. An average flow model for determining effects of three-dimensional roughness on partial hydrodynamic lubrication. J Lub Tech 1978;100(1):12. https://doi.org/10.1115/1.3453103.

[49] Patir N, Cheng HS. Application of average flow model to lubrication between rough sliding surfaces. J Lub Tech 1979;101(2):220. https://doi.org/10.1115/1.3453329.

[50] Peeken HJ, Knoll G, Rienäcker A, Lang J, Schönen R. On the numerical determination of flow factors. J Tribol 1997;119(2):259. https://doi.org/10.1115/1.2833178.

[51] Bartel D, Bobach L, Illner T, Deters L. Simulating transient wear characteristics of journal bearings subjected to mixed friction. Proc Inst Mech Eng J J Eng Tribol 2012;226(12):1095–108. https://doi.org/10.1177/1350650112454510.

[52] Kim TW, Cho YJ. The flow factors considering the elastic deformation for the rough surface with a non-Gaussian height distribution. Tribol Trans 2008;51(2):213–20. https://doi.org/10.1080/10402000701730502.

[53] Pusterhofer M, Bergmann P, Summer F, Grün F, Brand C. A novel approach for modeling surface effects in hydrodynamic lubrication. Lubricants 2018;6(1):27. https://doi.org/10.3390/lubricants6010027.

[54] Leighton M, Rahmani R, Rahnejat H. Surface-specific flow factors for prediction of friction of cross-hatched surfaces. Surf Topogr: Metrol Prop 2016;4(2):25002. https://doi.org/10.1088/2051-672X/4/2/025002.

[55] Jocsak J, Li Y, Tian T, Wong VW. Analyzing the effects of three-dimensional cylinder liner surface texture on ring-pack performance with a focus on honing groove cross-hatch angle. In: Proceedings of the 2005 fall technical conference of the ASME internal combustion engine division: presented at fall technical conference of the ASME internal combustion engine division, september 11 - 14, 2005, Ottawa, Ontario, Canada. New York, NY: ASME; 2005. p. 621–32.

[56] de Kraker A, van Ostayen RAJ, Rixen DJ. Development of a texture averaged Reynolds equation. Tribol Int 2010;43(11):2100–9. https://doi.org/10.1016/j.triboint.2010.06.001.

[57] de Kraker A, van Ostayen RAJ, van Beek A, Rixen DJ. A multiscale method modeling surface texture effects. J Tribol 2007;129(2):221. https://doi.org/10.1115/1.2540156.

[58] Ma C, Duan Y, Yu B, Sun J, Tu Q. The comprehensive effect of surface texture and roughness under hydrodynamic and mixed lubrication conditions. Proc Inst Mech Eng J J Eng Tribol 2017;231(10):1307–19. https://doi.org/10.1177/1350650117693146.

[59] Xie Y, Li Y, Suo S, Liu X, Li J, Wang Y. A mass-conservative average flow model based on finite element method for complex textured surfaces. Sci China Phys Mech Astron 2013;56(10):1909–19. https://doi.org/10.1007/s11433-013-5217-z.

[60] Profito FJ, Vlădescu S-C, Reddyhoff T, Dini D. Transient experimental and modelling studies of laser-textured micro-grooved surfaces with a focus on piston-ring cylinder liner contacts. Tribol Int 2017;113:125–36. https://doi.org/10.1016/j.triboint.2016.12.003.

[61] Profito FJ, Tomanik E, Zachariadis DC. Effect of cylinder liner wear on the mixed lubrication regime of TLOCRs. Tribol Int 2016;93:723–32. https://doi.org/10.1016/j.triboint.2015.01.004.

[62] Sander DE, Allmaier H. Starting and stopping behavior of worn journal bearings. Tribol Int 2018;127:478–88. https://doi.org/10.1016/j.triboint.2018.06.031.

[63] Sander DE, Allmaier H, Priebsch HH, Reich FM, Witt M, Skiadas A, et al. Edge loading and running-in wear in dynamically loaded journal bearings. Tribol Int 2015;92:395–403. https://doi.org/10.1016/j.triboint.2015.07.022.

[64] Sander DE, Allmaier H, Priebsch HH, Witt M, Skiadas A. Simulation of journal bearing friction in severe mixed lubrication – validation and effect of surface smoothing due to running-in. Tribol Int 2016;96:173–83. https://doi.org/10.1016/j.triboint.2015.12.024.

[65] Sander DE, Allmaier H, Priebsch H-H. Friction and wear in automotive journal bearings operating in today's severe conditions. In: Darji PH, editor. Advances in Tribology. InTech; 2016.

[66] König F, Ould Chaib A, Jacobs G, Sous C. A multiscale-approach for wear prediction in journal bearing systems – from wearing-in towards steady-state wear. Wear 2019;426–427:1203–11. https://doi.org/10.1016/j.wear.2019.01.036.

[67] Sheets B. Advanced modelling of the lubricated boundary friction coefficient. São Paulo, Brazil.

[68] Bartel D. Simulation von Tribosystemen: grundlagen und Anwendungen. Wiesbaden: Vieweg+Teubner Verlag/GWV Fachverlage GmbH Wiesbaden; 2010.

[69] Wu C, Zheng L. An average Reynolds equation for partial film lubrication with a contact factor. J Tribol 1989;111(1):188–91. https://doi.org/10.1115/1.3261872.

[70] Bonneau D, Fatu A, Souchet D. Mixed lubrication in hydrodynamic bearings. London, Hoboken, NJ: ISTE; 2014.

[71] Jakobsson B, Floberg L. The finite journal bearing considering vaporization: das Gleitlager von unendlicher Breite mit Verdampfung. Göteborg: Gumpert; 1957.

[72] Kalin M, Pogačnik A. Criteria and properties of the asperity peaks on 3D engineering surfaces. Wear 2013;308(1):95–104. https://doi.org/10.1016/j.wear.2013.09.010.

[73] Herbst HM. Theoretical modeling of the cylinder lubrication in internal combustion engines and its influence on piston slap induced noise, friction and wear. 2007.

[74] Bergmann P, Grün F, Gódor I, Stadler G, Maier-Kiener V. On the modelling of mixed lubrication of conformal contacts. Tribol Int 2018;125:220–36. https://doi.org/10.1016/j.triboint.2018.03.010.

[75] Isaksson P, Nilsson D, Larsson R, Almqvist A. The influence of surface roughness on friction in a flexible hybrid bearing. Proc Inst Mech Eng J J Eng Tribol 2011;225(10):975–85. https://doi.org/10.1177/1350650111417203.

[76] zum Gahr K-H. Microstructure and wear of materials. Amsterdam: Elsevier; 1987.

[77] Persson BNJ, Scaraggi M. Lubricated sliding dynamics: flow factors and Stribeck curve. Eur Phys J E (EPJ E), - Soft Matter 2011;34(10):113. https://doi.org/10.1140/epje/i2011-11113-9.

[78] Greenwood JA, Tripp JH. The contact of two nominally flat rough surfaces. Proc Inst Mech Eng 1970;185(1):625–33. https://doi.org/10.1243/PIME_PROC_1970_185_069_02.

[79] Almqvist A, Lukkassen D, Meidell A, Wall P. New concepts of homogenization applied in rough surface hydrodynamic lubrication. Int J Eng Sci 2007;45(1):139–54. https://doi.org/10.1016/j.ijengsci.2006.09.005.

[80] Rom M, Muller SA. Reduced basis method for the homogenized Reynolds equation Applied to textured surfaces. CiCP 2018;24(2). https://doi.org/10.4208/cicp.OA-2017-0121.

[81] Furustig J, Dobryden I, Almqvist A, Almqvist N, Larsson R. The measurement of wear using AFM and wear interpretation using a contact mechanics coupled wear model. Wear 2016;350–351:74–81. https://doi.org/10.1016/j.wear.2016.01.002.